Analytic solution to boundary integral computation of susceptibility induced magnetic field inhomogeneities

Stéphane Balac, Hugues Benoit-Catton, Thomas Lamotte, Christophe Odet

Analytic Solution to Boundary Integral Computation of Susceptibility Induced Magnetic Field Inhomogeneities

S. Balac*
MAPLY, UMR CNRS 5585
INSA de Lyon, 69621 Villeurbanne, France

H. Benoit-Catton, T. Lamotte and C. Odet
CREATIS, UMR CNRS 5515
INSA de Lyon, 69621 Villeurbanne, France

Abstract—A method to compute the magnetic field induced by susceptibility inhomogeneities in magnetic resonance imaging is presented. It is based on a boundary integral representation formulae. The integral is set over the surfaces between media of different magnetic susceptibilities. The computational procedure consists of approximating these surfaces with triangular mesh elements and using analytical expressions to compute the integral over each triangle. The proposed method supplies high accuracy and is easily paralleled. A detailed analysis for the convergence rate of the method is performed. Numerical results obtained for several samples, including a human head, are presented.

Keywords—Boundary integrals, Susceptibility artifacts, Magnetostatics.

1. INTRODUCTION

When a sample is magnetized by a static magnetic field, as during a magnetic resonance imaging (MRI) experiment, the magnetic field around the sample is distorted. The magnetic susceptibility distribution in the sample determines the local perturbation of the magnetic field. In MRI, differences in susceptibility between a metallic implant and the surrounding anatomic tissues, or between air and tissues, are one of the greatest sources of geometric distortions in the images, see [1,2] for instance. These distortions are harmful for applications that require accurate quantitative measurements from the images, see [3,4].

Since the knowledge of the static magnetic field perturbation is necessary to rectify distorted MR images, many studies deal with its quantification, see [5,6], and its computation. Analytic methods have been proposed to study simple geometries objects such as spheres or cylinders,

*Author to whom all correspondence should be addressed.
This work is in the scope of the scientific topics of the PRC-GdR ISIS Research Group of the French National Center for Scientific Research CNRS. This work has been also funded by the INSA Lyon. We want to thank B. Belaroussi for his contribution on the hollow ball results and F. Bellet for his help on the parallel implementation of the method.

see [1]. For more complex geometries, a precise computation of the magnetic field perturbation involves partial-differential equations derived from Maxwell's equations and requires the use of numerical methods. Among the classical numerical methods are the finite-difference method (FDM), the finite-element method (FEM), and the boundary elements method (BEM) (we refer to [7] for a comprehensive presentation of these numerical methods in electromagnetism). These methods have been widely used to compute the magnetic field perturbation generated by susceptibility inhomogeneities during an MRI experiment. For instance, Bhagwadien *et al.* [8] developed an iterative finite-difference method for computing the static field for arbitrary magnetic susceptibility distributions. Li *et al.* [9] used commercial finite-element software to compute the three-dimensional magnetic field in a human head. Based on the previous finite-element approach, Truong *et al.* [10] proposed a multiresolution computation of the magnetic field and its application to several anatomical models. Jenkinson *et al.* [11] proposed an approach based on a perturbation method which is adapted to a nonconductive object represented by rectangular voxels restricted to air and singular tissue. The boundary element method has been used by Hwang *et al.* [12] to simulate the magnetic field perturbation on trabecular bone MR images. The BEM is used as well by De Munck *et al.* [13] to compute distortions on MRI images from a human head. Yoder *et al.* [14] simplified the BEM approach in the case of homogeneous voxels perpendicular to the static field and integrated the computed field perturbation in a MRI simulator. The BEM relies on a computation over the interfaces between domains of different susceptibilities. The magnetic field perturbation is obtained through the resolution of a linear system whose coefficients are determined by evaluating surface integrals. In the quoted works, the surface integrals were approximated considering only small susceptibility values corresponding to anatomical tissues values.

In [15], Balac and Caloz present a method to compute the magnetic field induced by metallic bodies with high constant magnetic susceptibility (such as medical implants) based on an integral representation formula over the boundary of the body. The method uses analytic expressions to compute the integral over the flat panels of the boundary and a piecewise quadratic interpolation of the surface for the curved panels. It supplies both high accuracy and low computation time. In this paper, we generalize the method presented in [15] to deal with bodies composed of several domains of arbitrary magnetic susceptibilities. The magnetic field is computed through an explicit integral representation formula over the boundary interfaces between the interior domains. The advantages of our method compared to the FEM or to the FDM are numerous. First, the computation depends only on the interface boundaries between media of different susceptibilities so that the computational problem is reduced from a 3D problem to a 2D problem. Furthermore, in the FDM/FEM the exterior domain must be truncated and an approximation of the behavior of the field at infinity must be introduced on an artificial boundary. In our approach, as well as with the BEM, the behavior at infinity is always exactly satisfied. Finally, the FEM as the FDM or the BEM lead to large linear systems to be solved, whereas in the proposed method the solution is obtained pointwise by evaluating a surface integral. Our computational method assumes the interface boundaries between media of different susceptibilities are meshed in a collection of flat triangles. The advantage is that the surface integral can be evaluated exactly with no limitation on the susceptibility values or on the static field direction. The only approximation in the method stands in the way the true interfaces are approached by the union of flats triangles and the approximation error is controlled by the size of the triangles. Thus, the computation of susceptibility induced magnetic field inhomogeneities is done by a unique and accurate method with a low computation time for both soft tissues and metallic objects. Moreover, our method can be parallelized in a very simple and efficient way, the computation time being divided by a factor equal to the number of computation nodes.

Our paper is organized as follows. In Section 2, we formulate the magnetostatic problem and give the integral formula used to compute the magnetic field. Section 3 is devoted to the presentation of the computational method and to a detailed analysis of its accuracy. In Section 4, we

present results obtained with our computational method. The validation is done on a diamagnetic and a paramagnetic ball. The convergence rate and the computation time are discussed. Finally, results obtained on a hollow ball and on a human head are presented.

2. FORMULATION OF THE PROBLEM

2.1. The Magnetostatic Problem

We denote by Ω the domain filled by the whole sample. Ω is an open bounded domain in $\mathbb{R}^3$, whose boundary is denoted by Σ. We assume that Ω is the union of N domains Ω_i with distinct magnetic properties. For convenience, we denote by Ω_{N+1} the exterior domain. We denote by Σ_{ij} the common boundary to Ω_i and Ω_j, $1 \leq i < j \leq N+1$ (possibly we have $\Sigma_{ij} = \emptyset$) and set

$$\mathcal{I} = \left\{(i,j) \in \mathbb{N}^2 \mid 1 \leq i < j \leq N+1 \text{ and } \Sigma_{ij} \neq \emptyset\right\}.$$

We denote by $\partial\Omega_k$ the whole boundary of Ω_k, $k \in \{1, \ldots, N\}$.

The sample is assumed to be embedded in the magnetic field $\mathbf{B_0}$ of the MRI device. We consider $\mathbf{B_0}$ constant in intensity and direction. In this modeling, we neglect the effects of the RF field $\mathbf{B_1}$ of the MRI device on the static field inhomogeneities.

Let $\mathbf{B}$ be the total magnetic flux density and $\mathbf{H}$ be the total magnetic field intensity. The basic equations of magnetostatics are, see [16],

$$\begin{aligned} \operatorname{div} \mathbf{B} &= 0, \qquad \text{in } \mathbb{R}^3, \\ \mathbf{rot}\, \mathbf{H} &= 0, \qquad \text{in } \mathbb{R}^3. \end{aligned} \tag{1}$$

At a distance far from Ω the magnetic field tends to become homogeneous; we have

$$\lim_{P \to \infty} \mathbf{B}(P) = \mathbf{B_0}. \tag{2}$$

In the exterior region Ω_{N+1}, $\mathbf{H}$ and $\mathbf{B}$ are related through the relation

$$\mathbf{H} = \frac{1}{\mu_0}\mathbf{B}, \tag{3}$$

where μ_0 is the magnetic permeability of vacuum, while in Ω they are connected to the magnetization $\mathbf{M}$ by the relation

$$\mathbf{H} = \frac{1}{\mu_0}\mathbf{B} - \mathbf{M}. \tag{4}$$

For the magnetic flux induction $\mathbf{B'} = \mathbf{B} - \mathbf{B_0}$ the problem reads: find $\mathbf{B'}$ in the space $L^2(\mathbb{R}^3)^3$ such that

$$\begin{aligned} \operatorname{div} \mathbf{B'} &= \mu_0 \operatorname{\mathbf{rot}} \mathbf{M}, && \text{in } \mathbb{R}^3, && \\ \mathbf{rot}\, \mathbf{B'} &= 0, && \text{in each } \Omega_i, && i \in \{1, \ldots, N+1\}, \\ [\mathbf{B'} \wedge \mathbf{n}] &= \mu_0 \left[\mathbf{M} \wedge \mathbf{n}\right], && \text{at the interfaces } \Sigma_{ij}, && (i,j) \in \mathcal{I}, \end{aligned} \tag{5}$$

where $\mathbf{n}$ is the unit normal to Σ_{ij} from Ω_i to Ω_j and $[v]$ denotes the jump of v across the boundary Σ_{ij}: $[v] = v|_{\Omega_i} - v|_{\Omega_j}$. To deal with a well-posed problem, we still need to add some relation between the magnetization $\mathbf{M}$ and the field $\mathbf{B'}$.

The domains Ω_i are assumed to be isotropic linear paramagnetic or diamagnetic materials. In each domain Ω_i, the magnetization $\mathbf{M}$ is then related to the applied field $\mathbf{B_0}$ through the linear relation

$$\mathbf{M} = \frac{\chi_m^{(i)}}{\mu_0}\mathbf{B_0}, \tag{6}$$

where $\chi_m^{(i)}$ is the magnetic susceptibility in Ω_i. The first consequence of this assumption is that on each Ω_i we have $\mathbf{rot}\,\mathbf{M} = 0$. The second one is that the interface conditions in (5) take the form

$$[\mathbf{B}' \wedge \mathbf{n}] = \mathbf{j}_{\Sigma_{ij}}, \tag{7}$$

where

$$\mathbf{j}_{\Sigma_{ij}} = [\chi_m]_{\Sigma_{ij}} (\mathbf{B_0} \wedge \mathbf{n}) = \left(\chi_m^{(i)} - \chi_m^{(j)}\right) (\mathbf{B_0} \wedge \mathbf{n}). \tag{8}$$

We can check that $\operatorname{div} \mathbf{j}_{\Sigma_{ij}} = 0$, so that $\mathbf{j}_{\Sigma_{ij}}$ can be interpreted as a fictitious surface current density over the surface Σ_{ij}. Finally, we look for $\mathbf{B}'$ such that

$$\begin{aligned} \operatorname{div} \mathbf{B}' &= 0, && \text{in } \mathbb{R}^3, \\ \mathbf{rot}\, \mathbf{B}' &= 0, && \text{in each } \Omega_i, && i \in \{1, \dots, N+1\}, \\ [\mathbf{B}' \wedge \mathbf{n}] &= \mathbf{j}_{\Sigma_{ij}}, && \text{at the interfaces } \Sigma_{ij}, && (i,j) \in \mathcal{I}. \end{aligned} \tag{9}$$

2.2. The Integral Formula for the Magnetic Field

Our method originates from the Biot and Savart law that states the solution to problem (9) can be expressed as, see [16],

$$\mathbf{B}'(P) = \frac{1}{4\pi} \sum_{(i,j)\in\mathcal{I}} \iint_{\Sigma_{ij}} \mathbf{j}_{\Sigma_{ij}}(Q) \wedge \frac{\mathbf{r}(P,Q)}{r^3(P,Q)}\, \mathrm{d}\sigma_Q, \tag{10}$$

where $\mathbf{r}(P,Q) = \mathbf{PQ}$. This relation is valid in any point P that does not belong to any of the interfaces Σ_{ij}. However, it is not convenient for numerical purposes in its present form and we use the following vector identity to transform relation (10) in a more suitable form: if $\mathbf{u}$, $\mathbf{v}$, $\mathbf{w}$ denote three vectors in $\mathbb{R}^3$, we have

$$(\mathbf{v} \wedge \mathbf{w}) \wedge \mathbf{u} = (\mathbf{u} \cdot \mathbf{v})\, \mathbf{w} - (\mathbf{u} \cdot \mathbf{w})\, \mathbf{v}.$$

It follows that

$$(\mathbf{B_0} \wedge \mathbf{n}) \wedge \frac{\mathbf{r}(P,Q)}{r^3(P,Q)} = \left(\frac{\mathbf{r}(P,Q)}{r^3(P,Q)} \cdot \mathbf{B_0}\right) \mathbf{n} - \left(\frac{\mathbf{r}(P,Q)}{r^3(P,Q)} \cdot \mathbf{n}\right) \mathbf{B_0}$$

and the solution to problem (9) given by (10) is

$$\mathbf{B}'(P) = \frac{1}{4\pi} \sum_{(i,j)\in\mathcal{I}} [\chi_m]_{\Sigma_{ij}} \left\{ -\iint_{\Sigma_{ij}} \left(\frac{\mathbf{r}(P,Q)}{r^3(P,Q)} \cdot \mathbf{n}\right) \mathbf{B_0}\, \mathrm{d}\sigma_Q + \iint_{\Sigma_{ij}} \left(\frac{\mathbf{r}(P,Q)}{r^3(P,Q)} \cdot \mathbf{B_0}\right) \mathbf{n}\, \mathrm{d}\sigma_Q \right\}. \tag{11}$$

As the source magnetic field $\mathbf{B_0}$ is constant, the first integral term in (11) reads

$$\begin{aligned} &- \frac{1}{4\pi} \sum_{(i,j)\in\mathcal{I}} [\chi_m]_{\Sigma_{ij}} \iint_{\Sigma_{ij}} \left(\frac{\mathbf{r}(P,Q)}{r^3(P,Q)} \cdot \mathbf{n}\right) \mathbf{B_0}\, \mathrm{d}\sigma_Q \\ &= -\frac{1}{4\pi} \left(\sum_{(i,j)\in\mathcal{I}} [\chi_m]_{\Sigma_{ij}} \iint_{\Sigma_{ij}} \frac{\mathbf{r}(P,Q)}{r^3(P,Q)} \cdot \mathbf{n}\, \mathrm{d}\sigma_Q \right) \mathbf{B_0} \\ &= \begin{cases} \chi_m(P) \mathbf{B_0}, & \text{if } P \in \Omega, \\ 0, & \text{if } P \notin \Omega. \end{cases} \end{aligned} \tag{12}$$

Indeed, if S is a close surface then the integral

$$\mathcal{A}(P,S) = \frac{1}{4\pi} \iint_S \frac{\mathbf{r}(P,Q)}{r^3(P,Q)} \cdot \mathbf{n}\, \mathrm{d}\sigma_Q$$

is the so-called "solid angle" whose value is

$$\mathcal{A}(P,S) = \begin{cases} -1, & \text{if } P \in V, \\ 0, & \text{if } P \notin V, \end{cases}$$

where V denotes the domain enclosed in S.

Finally, the Biot and Savart integral (10) had been transformed into the following expressions. If P belongs to Ω but at none of the interfaces Σ_{ij}, then

$$\begin{aligned} \mathbf{B}'(P) &= \chi_m(P)\ \mathbf{B_0} + \frac{1}{4\pi} \sum_{(i,j)\in\mathcal{I}} [\chi_m]_{\Sigma_{ij}} \iint_{\Sigma_{ij}} \left(\frac{\mathbf{r}(P,Q)}{r^3(P,Q)} \cdot \mathbf{B_0} \right) \mathbf{n}\, \mathrm{d}\sigma_Q \\ &= \chi_m(P)\ \mathbf{B_0} + \frac{1}{4\pi} \sum_{k=1}^{N} \chi_m^{(k)} \iint_{\partial\Omega_k} \left(\frac{\mathbf{r}(P,Q)}{r^3(P,Q)} \cdot \mathbf{B_0} \right) \mathbf{n}\, \mathrm{d}\sigma_Q. \end{aligned} \tag{13}$$

If P belongs to one of the interface Σ_{ij}, then $\mathbf{B}(P)$ is undefined. The reason being that the magnetic induction is not continuous across boundaries of medium of different susceptibilities, see equations (5). If P belongs to the exterior domain Ω_{N+1}, then

$$\begin{aligned} \mathbf{B}'(P) &= \frac{1}{4\pi} \sum_{(i,j)\in\mathcal{I}} [\chi_m]_{\Sigma_{ij}} \iint_{\Sigma_{ij}} \left(\frac{\mathbf{r}(P,Q)}{r^3(P,Q)} \cdot \mathbf{B_0} \right) \mathbf{n}\, \mathrm{d}\sigma_Q \\ &= \frac{1}{4\pi} \sum_{k=1}^{N} \chi_m^{(k)} \iint_{\partial\Omega_k} \left(\frac{\mathbf{r}(P,Q)}{r^3(P,Q)} \cdot \mathbf{B_0} \right) \mathbf{n}\, \mathrm{d}\sigma_Q. \end{aligned} \tag{14}$$

Thus, in both cases, the computation of the magnetic field perturbation $\mathbf{B}'$ turned to the calculation of the following surface integrals over the boundaries $\partial\Omega_k,\ k = 1, \ldots, N$,

$$\mathcal{I}_k = \iint_{\partial\Omega_k} \left(\frac{\mathbf{r}(P,Q)}{r^3(P,Q)} \cdot \mathbf{B_0} \right) \mathbf{n}\, \mathrm{d}\sigma_Q. \tag{15}$$

3. THE COMPUTATIONAL METHOD

3.1. Overview of the Method

We assume that each boundary $\partial\Omega_k, k = 1, \ldots, N$, has a parameterization $F_k : D \longrightarrow \partial\Omega_k$, where D is a polygonal domain in the plane which is two times continuously differentiable (or that it can be decomposed in a union of smooth closed surfaces having this property). To the polygonal domain D, we associate a triangulation $\hat{T}_h$, $\hat{T}_h = \{\hat{K}_i,\ 1 \le i \le N\}$ where $\hat{K}_i$ are triangles in the plane. The mesh size h of the triangulation is defined by

$$h = \max_{1\le i\le N} \operatorname{diam}\left(\hat{K}_i\right), \qquad \text{where } \operatorname{diam}\left(\hat{K}_i\right) = \max_{P,Q\in\hat{K}_i} |P-Q|,$$

with $|\ |$ being the usual Euclidian norm. The parameters h and N are linked by the relation $N = \mathcal{O}(1/h^2)$. Without loss of generality, we can assume that the polygonal domain D is a right-angled, isosceles triangle and that the triangulation $\hat{T}_h$ of D is composed of N right-angled, isosceles triangles. A triangulation T_h of the surface $\partial\Omega_k$ can be obtained from the triangulation $\hat{T}_h$ of the polygonal domain D through the parameterization F, each element K in T_h (with vertices v_1, v_2, v_3) being the image of a triangle $\hat{K}$ in $\hat{T}_h$ (with vertices $\hat{v_1}, \hat{v_2}, \hat{v_3}$ such that $v_i = F(\hat{v}_i),\ i = 1, 2, 3$). Thus, we can write $\mathcal{I}_k$ as

$$\mathcal{I}_k(P) = \sum_{K\in T_h} \iint_K \left(\frac{\mathbf{r}(P,Q)}{r^3(P,Q)} \cdot \mathbf{B_0} \right) \mathbf{n}\, \mathrm{d}\sigma_Q. \tag{16}$$

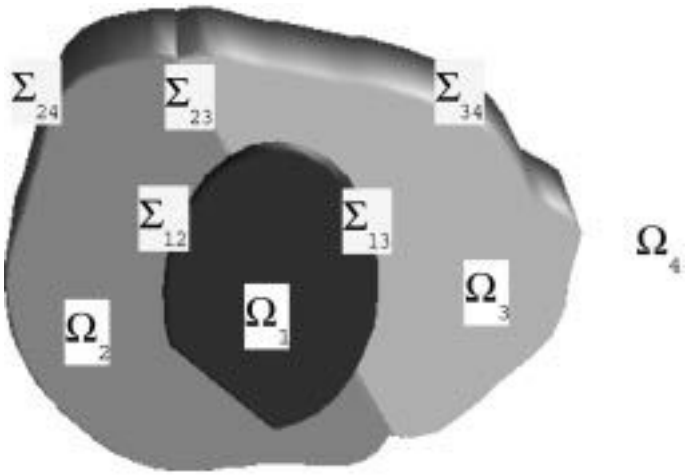

Figure 1. The situation under consideration.

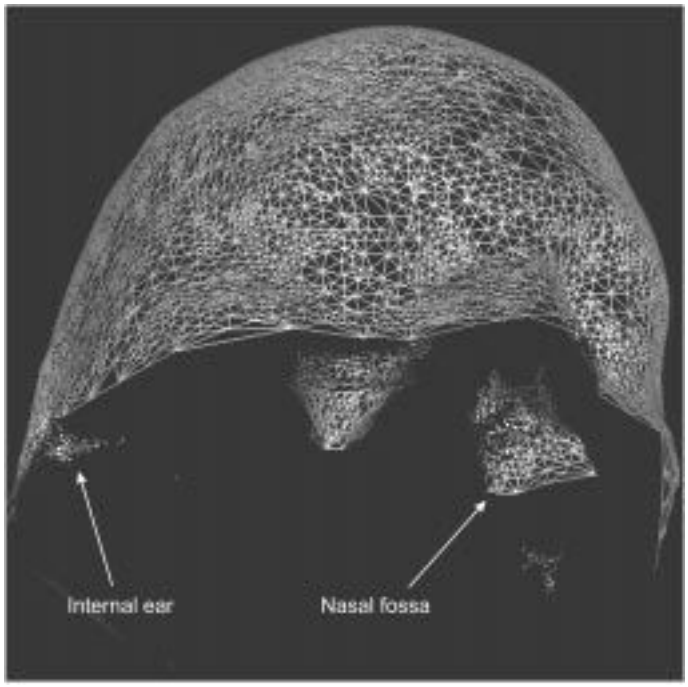

Figure 2. Interface between a head and air defined by a mesh of 31064 triangles.

As the elements K in T_h are curved triangles in the space, it is not in general possible to proceed to an exact calculation of $\mathcal{I}_k$. We then compute an approximation of $\mathcal{I}_k$ by using a piecewise linear interpolation of the surface $\partial\Omega_k$. The approximated surface $\widetilde{\partial\Omega}_k$ will be composed of flat triangles $\tilde{K}$ in the space that are obtained as the linear interpolants of the curved triangular elements K in T_h. We denote by $\tilde{T}_h$ the triangulation of $\widetilde{\partial\Omega}_k$ obtained in this way. We have

$$\partial\Omega_k = \bigcup_{K\in T_h} K \approx \bigcup_{\tilde{K}\in\tilde{T}_h} \tilde{K} = \widetilde{\partial\Omega}_k. \tag{17}$$

If $K \in T_h$ is the image of the triangle $\hat{K} \in \hat{T}_h$ through the parameterization F, the corresponding triangle $\tilde{K} \in \tilde{T}_h$ is the image of $\hat{K}$ through the linear interpolant $\tilde{F}_K$ of F over K. It follows that the integral $\mathcal{I}_k$ over the boundary $\partial\Omega_k$ can be approximated by the following integral over the

approximate boundary $\widetilde{\partial\Omega}_k$:

$$\tilde{\mathcal{I}}_k(P) = \iint_{\widetilde{\partial\Omega}_k} \left(\frac{\mathbf{r}(P,Q)}{r^3(P,Q)} \cdot \mathbf{B_0} \right) \mathbf{n} \, \mathrm{d}\sigma_Q = \sum_{\tilde{K} \in \tilde{T}_h} \iint_{\tilde{K}} \left(\frac{\mathbf{r}(P,Q)}{r^3(P,Q)} \cdot \mathbf{B_0} \right) \mathbf{n} \, \mathrm{d}\sigma_Q. \tag{18}$$

Since the triangles $\tilde{K} \in \tilde{T}_h$ are flat, the normal vector $\mathbf{n}$ is constant on each triangle $\tilde{K}$. Moreover, as the magnetic field $\mathbf{B_0}$ is constant in strength and direction, $\tilde{\mathcal{I}}_k$ may be written as

$$\tilde{\mathcal{I}}_k(P) = \sum_{\tilde{K} \in \tilde{T}_h} \left(\mathbf{B_0} \cdot \left(\iint_{\tilde{K}} \frac{\mathbf{r}(P,Q)}{r^3(P,Q)} \, \mathrm{d}\sigma_Q \right) \, \mathbf{n} \right). \tag{19}$$

Thus, the problem now reduces to the computation of the following integral over each triangle $\tilde{K} \in \tilde{T}_h$:

$$\tilde{\mathcal{J}}_K(P) = \iint_{\tilde{K}} \frac{\mathbf{r}(P,Q)}{r^3(P,Q)} \, \mathrm{d}\sigma_Q. \tag{20}$$

There are several ways to compute analytically this integral, see [17,18] for instance. Of course, in the implementation of the method, we only use the triangulation $\tilde{T}_h$ of $\widetilde{\partial\Omega}_k$ and never refer to the exact boundary $\partial\Omega_k$, nor to the triangulations T_h and $\hat{T}_h$. The triangulation $\tilde{T}_h$ is generated using standard commercial meshing softwares, see Figure 2.

The only approximation in the method stands in the way the surface $\partial\Omega_k$ is approached by the surface $\widetilde{\partial\Omega}_k$. It is obvious that the approximation of the surface $\partial\Omega_k$ becomes more and more accurate as the number of triangles increases, and therefore, that $\mathcal{I}_k$ tends to $\tilde{\mathcal{I}}_k$ when h tends to zero. In the next section, we investigate the way $\mathcal{I}_k$ converges to $\tilde{\mathcal{I}}_k$, that is to say how the approximation error is controlled by the size of the triangles (or equivalently by the number of triangles).

3.2. Error Estimate for the Method

In order to study the approximation error in computing the magnetic field perturbation with the method presented in the previous section, we follow the general method presented in [19]. A similar error analysis is presented in [15] when the surface is approached using piecewise quadratic interpolation. The approximation error related to the computation of the integral over the interface $\partial\Omega_k$ is given by

$$E_k(P) = \iint_{\partial\Omega_k} \Phi(P,Q) \, \mathbf{n} \, \mathrm{d}\sigma_Q - \iint_{\widetilde{\partial\Omega}_k} \Phi(P,Q) \, \mathbf{n} \, \mathrm{d}\sigma_Q, \tag{21}$$

where we have set

$$\Phi : (P,Q) \in \mathbb{R}^3 \longmapsto \frac{\mathbf{r}(P,Q)}{r^3(P,Q)} \cdot \mathbf{B_0}. \tag{22}$$

With the notations of Section 3.1, it is clear that the error estimate consists of studying

$$E_k(P) = \sum_{\hat{K} \in \hat{T}_h} \left\{ \iint_{F(\hat{K})} \Phi(P,Q) \, \mathbf{n} \, \mathrm{d}\sigma_Q - \iint_{\tilde{F}(\hat{K})} \Phi(P,Q) \, \mathbf{n} \, \mathrm{d}\sigma_Q \right\} = \sum_{\hat{K} \in \hat{T}_h} e_{\hat{K}}(P). \tag{23}$$

Our goal is now to carefully overestimate the local error $e_{\hat{K}}(P)$.

We introduce the reference element σ defined by $\sigma = \{(s,t) \in [0,1]^2 \mid 0 \leq s+t \leq 1\}$ and denote by ρ_1, ρ_2, and ρ_3 its vertices, see Figure 3. For all $K \in T_h$ with $K = F(\hat{K})$, we define the mapping m_K by

$$\forall \, (s,t) \in \sigma, \qquad m_K(s,t) = F(L_1(s,t)\hat{v}_1 + L_2(s,t)\hat{v}_2 + L_3(s,t)\hat{v}_3), \tag{24}$$

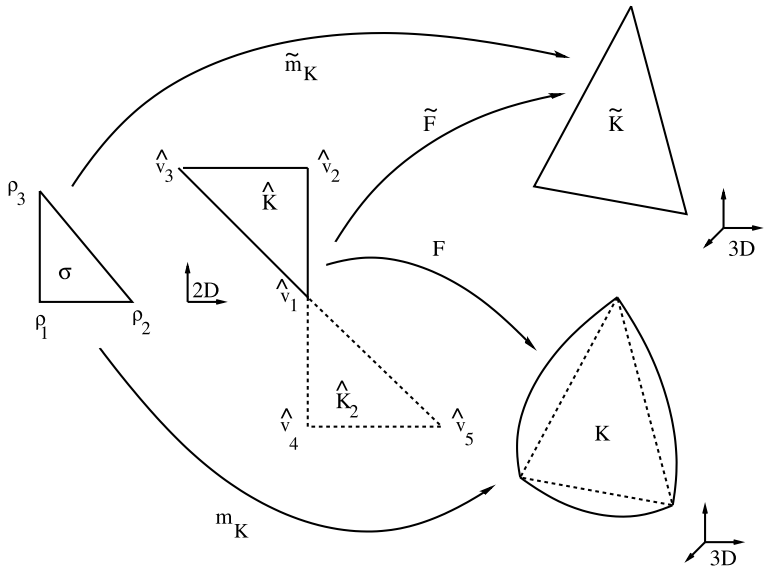

Figure 3. Notation used in the error analysis.

where L_j, $j \in \{1,2,3\}$, denote the j^{th} basis function for the linear Lagrange interpolation over the unit simplex σ. Namely, for all $(s,t) \in \sigma$, we have

$$L_1(s,t) = 1-(s+t), \qquad L_2(s,t) = s, \qquad L_3(s,t) = t. \tag{25}$$

We denote by $x^i(s,t)$ the i^{th} component of $m_K(s,t)$ for $i \in \{1,2,3\}$. A straightforward calculation shows that $\tilde{K}$ is the image of σ by $\tilde{m}_K$ where the mapping $\tilde{m}_K$ is defined for all $(s,t) \in \sigma$ by

$$\tilde{m}_K(s,t) = \tilde{F}(L_1(s,t)\hat{v}_1 + L_2(s,t)\hat{v}_2 + L_3(s,t)\hat{v}_3) = \sum_{j=1}^{3} m_K(\rho_j)\ L_j(s,t). \tag{26}$$

If we denote by $\tilde{x}^i(s,t)$ the i^{th} component of $\tilde{m}_K(s,t)$, we have

$$\tilde{x}^i(s,t) = \sum_{j=1}^{3} x^i(\rho_j)\ L_j(s,t) = x^i(0,0)L_1(s,t) + x^i(1,0)L_2(s,t) + x^i(0,1)L_3(s,t). \tag{27}$$

In the following, we refer to the derivation with respect to the variable s by ∂_s or by the subscript s and set $\Phi_P(.) = \Phi(P,.)$. Introducing the change in variables defined by m_K and $\tilde{m}_K$, the local error $e_{\hat{K}}(P)$ may be written as

$$\begin{aligned} e_{\hat{K}}(P) &= \iint_{F(\hat{K})} \Phi(P,Q)\,\mathbf{n}\,\mathrm{d}\sigma_Q - \iint_{\tilde{F}(\hat{K})} \Phi(P,Q)\,\mathbf{n}\,\mathrm{d}\sigma_Q \\ &= \iint_{\sigma} \big(\Phi_P(m_K(s,t))\ \ (\partial_s m_K(s,t) \wedge \partial_t m_K(s,t)) \\ &\quad -\Phi_P(\tilde{m}_K(s,t))\,(\partial_s \tilde{m}_K(s,t) \wedge \partial_t \tilde{m}_K(s,t))\big)\ \mathrm{d}s\,\mathrm{d}t. \end{aligned} \tag{28}$$

The local error is decomposed into two terms

$$e_{\hat{K}}(P) = e_{1,\hat{K}}(P) + e_{2,\hat{K}}(P), \tag{29}$$

where

$$\begin{aligned} e_{1,\hat{K}}(P) = \iint_{\sigma} &\Phi_P(m_K(s,t)) \\ &\times (\partial_s m_K(s,t) \wedge \partial_t m_K(s,t) - \partial_s \tilde{m}_K(s,t) \wedge \partial_t \tilde{m}_K(s,t))\ \mathrm{d}s\,\mathrm{d}t, \end{aligned} \tag{30}$$

$$e_{2,\hat{K}}(P) = \iint_{\sigma} (\Phi_P(m_K(s,t)) - \Phi_P(\tilde{m}_K(s,t))) \times (\partial_s \tilde{m}_K(s,t) \wedge \partial_t \tilde{m}_K(s,t)) \, \mathrm{d}s \, \mathrm{d}t. \tag{31}$$

The first term gives the error when approximating the normal to the surface and the second one the error when computing the integrand on the approximated surface. We start with an estimate on each triangle between the normal to the surface and the normal to the approximated surface.

LEMMA 1. *For each triangle $K \in T_h$ and for all $(s,t) \in \sigma$, we have*

$$\partial_s m_K(s,t) \wedge \partial_t m_K(s,t) - \partial_s \tilde{m}_K(s,t) \wedge \partial_t \tilde{m}_K(s,t) = \mathcal{O}\left(h^3\right).$$

PROOF. We set $e_n(s,t) = \partial_s m_K(s,t) \wedge \partial_t m_K(s,t) - \partial_s \tilde{m}_K(s,t) \wedge \partial_t \tilde{m}_K(s,t)$. The component i of e_n reads

$$e_n^i(s,t) = x_s^{i+1}(s,t)x_t^{i+2}(s,t) - x_s^{i+2}(s,t)x_t^{i+1}(s,t) - \tilde{x}_s^{i+1}(s,t)\tilde{x}_t^{i+2}(s,t) + \tilde{x}_s^{i+2}(s,t)\tilde{x}_t^{i+1}(s,t), \tag{32}$$

for $i \in \{1,2,3\}$ with the convention $i+2 = 1$ if $i = 2$ and $i+1 = 1$, $i+2 = 2$ if $i = 3$. To get estimates for $e_n(s,t)$, we need to develop the functions $x^i(s,t)$ and $\tilde{x}^i(s,t)$ according to Taylor formula in a neighborhood of $(0,0)$. It is important to note that the first derivatives of x^i behave in $\mathcal{O}(h)$, the second derivatives of x^i behave in $\mathcal{O}(h^2)$ and so on. Indeed, the derivatives of x^i with respect to (s,t) give rise to formula involving $\hat{v}_2 - \hat{v}_1$ and $\hat{v}_3 - \hat{v}_1$. For example,

$$\begin{aligned} \partial_s x^i(s,t) &= \nabla F^i((1-s-t)\hat{v}_1 + s\hat{v}_2 + t\hat{v}_3) \cdot (\hat{v}_2 - \hat{v}_1) = \mathcal{O}(h), \\ \partial_t x^i(s,t) &= \nabla F^i((1-s-t)\hat{v}_1 + s\hat{v}_2 + t\hat{v}_3) \cdot (\hat{v}_3 - \hat{v}_1) = \mathcal{O}(h). \end{aligned}$$

The Taylor expansion of $x^i(s,t)$ in a neighborhood of $(0,0)$ gives

$$x^i(s,t) = x^i(0,0) + sx_s^i(0,0) + tx_t^i(0,0) + \frac{1}{2}s^2x_{ss}^i(0,0) + stx_{st}^i(0,0) + \frac{1}{2}t^2x_{tt}^i(0,0) + \mathcal{O}\left(h^3\right). \tag{33}$$

Then the function $\tilde{x}^i(s,t)$ in (27) admits the development

$$\begin{aligned} \tilde{x}^i(s,t) &= x^i(0,0)L_1(s,t) + x^i(1,0)L_2(s,t) + x^i(0,1)L_3(s,t) \\ &= x^i(0,0)L_1(s,t) + \left(x^i(0,0) + x_s^i(0,0) + \frac{1}{2}x_{ss}^i(0,0) + \mathcal{O}\left(h^3\right)\right)L_2(s,t) \\ &\quad + \left(x^i(0,0) + x_t^i(0,0) + \frac{1}{2}x_{tt}^i(0,0) + \mathcal{O}\left(h^3\right)\right)L_3(s,t) \\ &= x^i(0,0) + sx_s^i(0,0) + tx_t^i(0,0) + \frac{1}{2}sx_{ss}^i(0,0) + \frac{1}{2}tx_{tt}^i(0,0) + \mathcal{O}\left(h^3\right). \end{aligned} \tag{34}$$

We make the difference $x^i(s,t) - \tilde{x}^i(s,t)$ in (33) and (34) to obtain

$$x^i(s,t) = \tilde{x}^i(s,t) + H^i(s,t) + \mathcal{O}\left(h^3\right), \tag{35}$$

where

$$H^i(s,t) = \frac{1}{2}\left(\left(s^2 - s\right)x_{ss}^i(0,0) + 2stx_{st}^i(0,0) + \left(t^2 - t\right)x_{tt}^i(0,0)\right) \tag{36}$$

behaves in $\mathcal{O}(h^2)$. Equation (35) permits us to express $e_n^i(s,t)$ as

$$e_n^i(s,t) = E_3^i(s,t) + \mathcal{O}\left(h^4\right), \tag{37}$$

where

$$\begin{aligned} E_3^i(s,t) = x_s^{i+1}(0,0)H_t^{i+2}(s,t) + x_t^{i+2}(0,0)H_s^{i+1}(s,t) \\ -x_s^{i+2}(0,0)H_t^{i+1}(s,t) - x_t^{i+1}(0,0)H_s^{i+2}(s,t) \end{aligned} \tag{38}$$

is a collection of term which are of order 3 in h. ∎

The next step in our error analysis uses the notion of *pair of symmetric triangles* introduced by Chien in [19]. We call a pair of symmetric triangles, two triangles $\hat{K}_1, \hat{K}_2 \in \hat{T}_h$ with vertices $\hat{v}_1, \hat{v}_2, \hat{v}_3$ and $\hat{v}_1, \hat{v}_4, \hat{v}_5$, respectively, having the following property, see Figure 3,

$$\begin{aligned} \hat{v}_1 - \hat{v}_2 &= -(\hat{v}_1 - \hat{v}_4), \\ \hat{v}_1 - \hat{v}_3 &= -(\hat{v}_1 - \hat{v}_5). \end{aligned} \tag{39}$$

If the triangulation $\hat{T}_h$ of the polygonal domain D (assumed to be a right-angled isosceles triangle) is composed of $N = \eta^2$ right-angled, isosceles triangles, then it is shown in [15] that there exists $(1/2)(\eta^2 - \eta)$ pairs of symmetric triangles and η unmatched triangles if η is odd and there exists $(1/2)(\eta^2 - 3\eta + 2)$ pairs of symmetric triangles and $3\eta - 2$ unmatched triangles if η is even. The key result in our error analysis is given in Lemma 2. It states that a cancellation happens among the local error terms from two symmetric triangles.

LEMMA 2. *Let $\hat{K}_1 \in \hat{T}_h$ and $\hat{K}_2 \in \hat{T}_h$ be a pair of symmetric triangles, then*

$$E_3^i(s,t)\big|_{\hat{K}_1} = -E_3^i(s,t)\big|_{\hat{K}_2}, \qquad \forall\,(s,t) \in \sigma. \tag{40}$$

PROOF. Let $\hat{v}_1, \hat{v}_2, \hat{v}_3$ and $\hat{v}_1, \hat{v}_4, \hat{v}_5$ be the vertices of the two triangles $\hat{K}_1$ and $\hat{K}_2$ as shown in Figure 3. Let (a_i, b_i) denote the coordinates of $\hat{v}_i$. We have

$$\begin{aligned} a_1 - a_2 &= a_4 - a_1, \qquad & b_1 - b_2 &= b_4 - b_1, \\ a_1 - a_3 &= a_5 - a_1, \qquad & b_1 - b_3 &= b_5 - b_1. \end{aligned} \tag{41}$$

Then for all $i \in \{1, 2, 3\}$,

$$\begin{aligned} \partial_s x^i(0,0)\big|_{\hat{K}_1} &= (a_3 - a_1)\ \partial_1 F^i(a_1, b_1) + (b_3 - b_1)\ \partial_2 F^i(a_1, b_1) \\ &= -(a_5 - a_1)\ \partial_1 F^i(a_1, b_1) - (b_5 - b_1)\ \partial_2 F^i(a_1, b_1) \\ &= -\partial_s x^i(0,0)\big|_{\hat{K}_2}. \end{aligned} \tag{42}$$

A similar development leads to $\partial_t x^i(0,0)|_{\hat{K}_1} = -\partial_t x^i(0,0)|_{\hat{K}_2}$ and

$$\partial^2_{ss}\ x^i(0,0)\big|_{\hat{K}_1} = \partial^2_{ss}\ x^i(0,0)\big|_{\hat{K}_2}, \qquad \partial^2_{st}\ x^i(0,0)\big|_{\hat{K}_1} = \partial^2_{st}\ x^i(0,0)\big|_{\hat{K}_2}, \tag{43}$$

$$\partial^2_{tt}\ x^i(0,0)\big|_{\hat{K}_1} = \partial^2_{tt}\ x^i(0,0)\big|_{\hat{K}_2}. \tag{44}$$

This last result combined with (36) shows that $H_3^i(s,t)|_{\hat{K}_1} = H_3^i(s,t)|_{\hat{K}_2}$. The result given in the lemma is then obvious from (38) and (43),(44). ∎

LEMMA 3. *The global error $E_1(P) = \sum_{\hat{K} \in \hat{T}_h} e_{1,\hat{K}}(P)$ behaves in $\mathcal{O}(h^2)$.*

PROOF. The local error $e_{1,\hat{K}}$ on the element K is given by (30). A Taylor expansion of Φ_P $(m_K(s,t))$ at $(s,t) = (0,0)$ leads to

$$\Phi_P(m_K(s,t)) = \Phi_P(m_K(0,0)) + \mathcal{O}(h). \tag{45}$$

Using Lemma 1 and equation (37), we get the following expression for the i^{th} component of $e_{1,\hat{K}}$:

$$e^i_{1,\hat{K}}(P) = \int_\sigma \Phi_P(m_K(0,0))\ E_3^i(s,t)\ \mathrm{d}s\,\mathrm{d}t + \mathcal{O}\left(h^4\right). \tag{46}$$

Due to pairs of symmetric triangles, cancellation will occur among the terms contributing to the error. Let us consider a pair of symmetric triangles $\hat{K}_1$ and $\hat{K}_2$ and their corresponding images

K_1 and K_2 in T_h. We have $\Phi_P(m_{K_1}(0,0)) = \Phi_P(m_{K_2}(0,0))$ and from Lemma 2, $E_3^i(s,t)|_{\hat{K}_1} = -E_3^i(s,t)|_{\hat{K}_2}$. It follows that the quantity

$$\int_\sigma \Phi_P(m_K(0,0))\ E_3^i(s,t)\ \mathrm{d}s\,\mathrm{d}t \tag{47}$$

from two symmetric triangles cancels giving

$$e^i_{1,\hat{K}_1} + e^i_{1,\hat{K}_2} = \mathcal{O}\left(h^4\right). \tag{48}$$

To conclude, we use the assumption made on the structured triangulation of D. We split the global error E_1 into two sums. One corresponding to the pairs of symmetric triangles for which the local error behaves in $\mathcal{O}(h^4)$. The number of pairs of symmetric triangles is proportional to $\eta^2 = N$ and behaves in $\mathcal{O}(1/h^2)$. Thus, this sum over the pairs of symmetric triangles behaves in $\mathcal{O}(h^2)$. The second sum corresponds to the triangles that cannot be matched for which the local error behaves in $\mathcal{O}(h^3)$. The numbers of such triangles is proportional to $\eta = \sqrt{N}$ and behaves in $\mathcal{O}(1/h)$. Thus, this sum over the unmatched triangles behaves in $\mathcal{O}(h^2)$ as well. In other terms, we write

$$\begin{aligned} E_1(P) &= \sum_{\hat{K}\in\hat{T}_h} e_{1,\hat{K}}(P) = \sum_{\substack{\text{matched}\\ \text{triangles}}} e_{1,\hat{K}}(P) \quad + \sum_{\substack{\text{unmatched}\\ \text{triangles}}} e_{1,\hat{K}}(P) \\ &= \mathcal{O}\left(\eta^2\right)\ \mathcal{O}\left(h^4\right) + \mathcal{O}(\eta)\ \mathcal{O}\left(h^3\right) \\ &= \mathcal{O}\left(h^{-2}\right)\mathcal{O}\left(h^4\right) + \mathcal{O}\left(h^{-1}\right)\mathcal{O}\left(h^3\right) = \mathcal{O}\left(h^2\right). \end{aligned} \tag{49}$$

∎

Lemma 4. *The global error $E_2(P) = \sum_{\hat{K}\in\hat{T}_h} e_{2,\hat{K}}(P)$ behaves in $\mathcal{O}(h^2)$.*

Proof. The local error $e_{2,\hat{K}}$ on the element $\hat{K}$ is given by (30). A Taylor expansion of Φ_P $(m_K(s,t))$ at $(s,t) = (0,0)$ leads to

$$\begin{aligned} \Phi_P(m_K(s,t)) &= \Phi_P(m_K(0,0)) + s\ \nabla\Phi_P(m_K(0,0)) \\ &\cdot\partial_s m_K(0,0) + t\ \nabla\Phi_P(m_K(0,0))\cdot\partial_t m_K(0,0) + \mathcal{O}\left(h^2\right), \end{aligned} \tag{50}$$

whereas a Taylor expansion of $\Phi_P(\tilde{m}_K(s,t))$ at $(s,t) = (0,0)$ leads to

$$\begin{aligned} \Phi_P(\tilde{m}_K(s,t)) &= \Phi_P(\tilde{m}_K(0,0)) + s\ \nabla\Phi_P(\tilde{m}_K(0,0)) \\ &\cdot\partial_s \tilde{m}_K(0,0) + t\nabla\Phi_P(\tilde{m}_K(0,0))\cdot\partial_t\tilde{m}_K(0,0) + \mathcal{O}\left(h^2\right). \end{aligned} \tag{51}$$

We have $\tilde{m}_K(0,0) = m_K(0,0)$ and

$$\partial_s m_K(0,0) = \partial_s\tilde{m}_K(0,0) + \mathcal{O}\left(h^2\right), \qquad \partial_t m_K(0,0) = \partial_t\tilde{m}_K(0,0) + \mathcal{O}\left(h^2\right).$$

It follows that $\Phi_P(m_K(s,t)) - \Phi_P(\tilde{m}_K(s,t)) = \mathcal{O}(h^2)$. As well,

$$\partial_s\tilde{m}_K(s,t)\wedge\partial_t\tilde{m}_K(s,t) = \partial_s\tilde{m}_K(0,0)\wedge\partial_t\tilde{m}_K(0,0) + \mathcal{O}\left(h^3\right) = \mathcal{O}\left(h^2\right). \tag{52}$$

Thus, the local error $e_{2,\hat{K}}$ behaves in $\mathcal{O}(h^4)$ and the sum over the $N = \mathcal{O}(h^2)$ triangles of the triangulation, gives $E_2(P) = \mathcal{O}(h^2)$. ∎

Collecting the results of both Lemmas 3 and 4, we easily deduce Proposition 1.

Proposition 1. *The error $E_k(P)$ in approximating*

$$\mathcal{I}_k(P) = \iint_{\partial\Omega_k}\left(\frac{\mathbf{r}(P,Q)}{r^3(P,Q)}\cdot\mathbf{B_0}\right)\mathbf{n}\,d\sigma_Q, \qquad \text{by } \tilde{\mathcal{I}}_k(P) = \iint_{\widetilde{\partial\Omega}_k}\left(\frac{\mathbf{r}(P,Q)}{r^3(P,Q)}\cdot\mathbf{B_0}\right)\mathbf{n}\,d\sigma_Q$$

as presented in Section 3.1 behaves in $\mathcal{O}(h^2)$ where h is the mesh size of the triangulation of $\widetilde{\partial\Omega}_k$.

So far we have fixed the point P and got estimates for the error $E_k(P)$. We know that the integrand Φ_P behaves like $1/d^2$ where d is the distance from P to the interface $\partial\Omega_k$. Thus, if the point P is at a distance $O(h)$ from the interface $\partial\Omega_k$, then $E_k(P) = \mathcal{O}(1)$. That means that for a given triangulation of the interface $\partial\Omega_k$, the error is not proportional to h^2 anymore when P is very close to the interface. This lack of accuracy of the method for points very close to the interface is not so harmful since these points are in an area where the approximation of the interface $\partial\Omega_k$ by $\widetilde{\partial\Omega}_k$ leads to uncertainty on their belonging to the domain Ω_k.

4. RESULTS

In this section, we first validate the accuracy of the method and illustrate some of its properties in the case where the sample is a ball made of diamagnetic or paramagnetic material. For this simple geometry, an analytical expression for the induced magnetic field is available, see [16] for instance. As well, we illustrate the convergence rate of the method by varying the mesh resolution of the ball boundary and give results on the computation time obtained on a single computer and on a computer cluster. Finally, we present results obtained on a hollow ball and on a human head.

4.1. Validation of the Method

The proposed method is validated with the case of a ball for which the exact values of the induced magnetic field is known, see [16]. The ball has a radius of 3 cm and is embedded in a magnetic field $\mathbf{B_0}$ of 1 Tesla. The ball boundary is meshed using 10080 triangles. We have tested two different materials for the ball: one with diamagnetic properties ($\chi_m = -9.05\ 10^{-6}$) and the other one with paramagnetic properties ($\chi_m = 10^{-4}$). We have computed the magnetic field perturbation along a scan line oriented perpendicularly to the static field $\mathbf{B_0}$ and passing through the center of the ball. We observe in the two cases that the numerical solutions and the exact one coincide. For instance, Figure 4 shows the component of the induced magnetic field along $\mathbf{B_0}$ in the case of the paramagnetic ball. The error between the numerically computed field and the exact one rapidly decreases as the distance from the boundary increases. The maximal error is located on the vicinity of the object boundary but is lower than 0.6 percent of the computed field for both materials: $0.018\,\mu T$ for the diamagnetic material and $0.19\ \mu T$ for the paramagnetic one (the error is depicted in Figure 5). First, we can notice that the relative error does not depend on the magnetic material involved since our method does not used any approximation nor assumption on the susceptibility range of values. Furthermore, the only approximation of the method lies in the way the interfaces between domains of different susceptibilities is approached using the mesh. This explains why the error is larger close to the boundary than far away from it. The defect in the surface approximation is greater for a point close to the boundary than for a point at a large distance of it. This phenomenon is in complete accordance with the analysis of the error behavior for our method presented in Section 3.2.

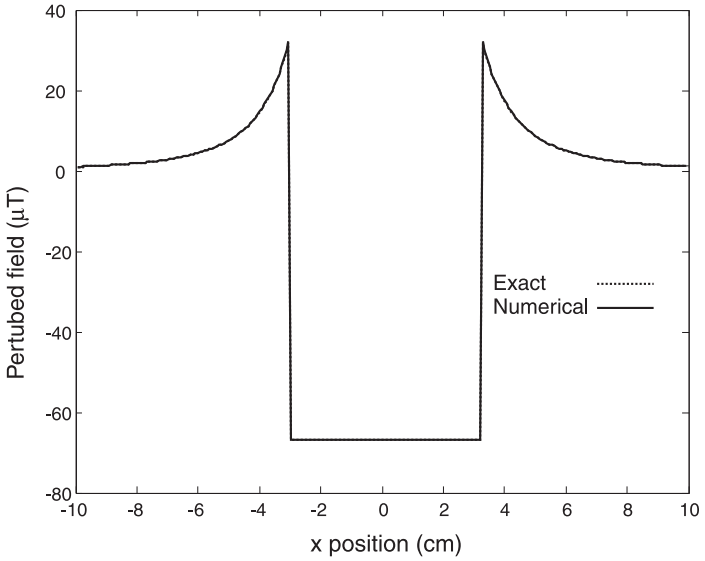

Figure 4. Magnetic field perturbation along a scan line oriented in a direction orthogonal to the magnetic field $\mathbf{B_0}$ (1 T.) and passing through the center of a paramagnetic ball ($\chi_m = 4\,10^{-3}$) of radius 3 cm. The numerical computation is done using 10080 triangles for the mesh of the ball surface.

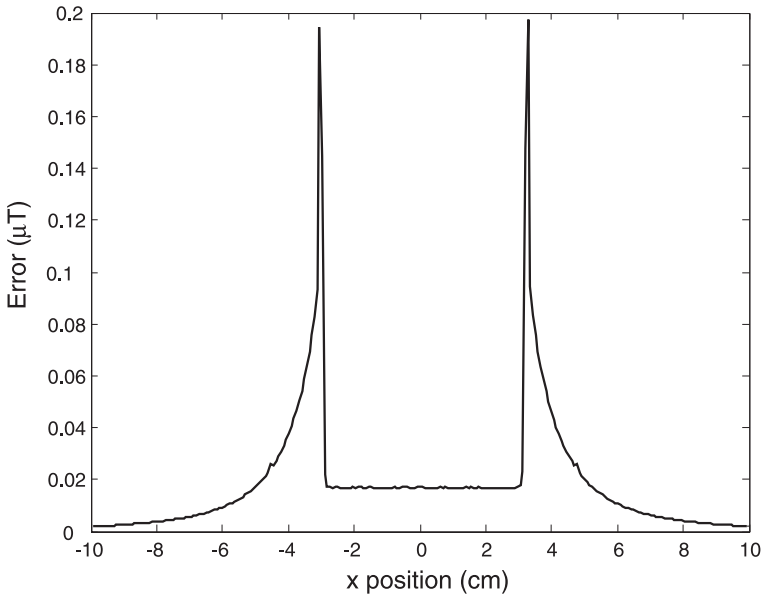

Figure 5. Difference between the exact and the numerically computed magnetic field perturbation in the situation of Figure 4.

4.2. Convergence Rate

To illustrate the behavior of the method as the number of triangles increases, we consider a point P at different distances from the center of the ball. The magnetic field perturbation $\mathbf{B}'$ is computed with meshes having an increasing number of triangles from 48 to 10080. We calculate in each case the error between the exact and the numerically computed magnetic field perturbation $\mathbf{B}'$. In Figures 6 and 7, we present the logarithm of the error E versus the logarithm of the number N of triangles for points chosen outside the ball (see Figure 6) and points chosen inside the ball (see Figure 7). In the two cases, the error is proportional to $1\,/\,N$ or equivalently to $h^{\,2}$.

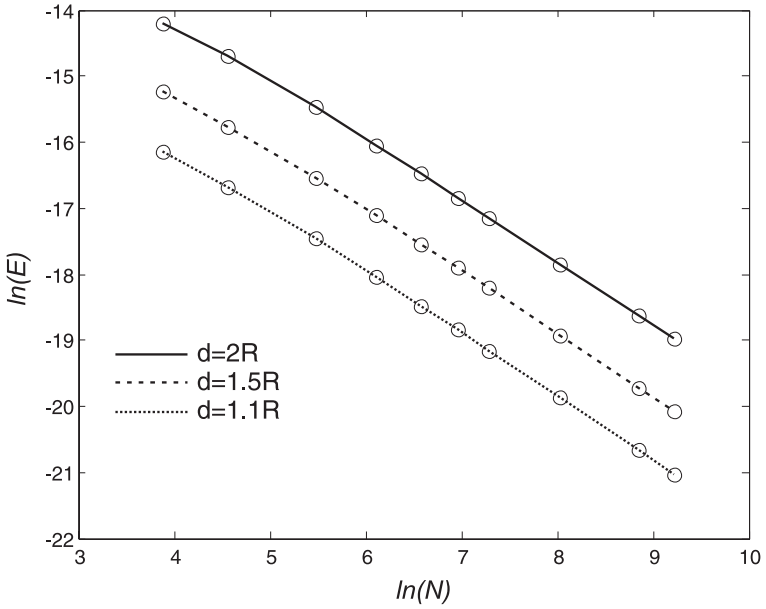

Figure 6. Logarithm of error between the exact and the numerically computed magnetic field perturbation as a function of the logarithm of the number of triangles for points outside the ball and located at different distances from the center of the ball of radius R.

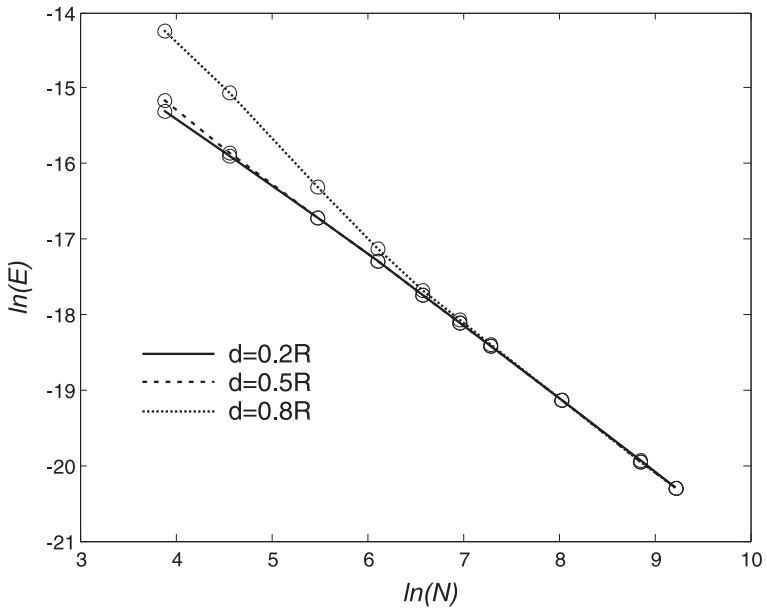

Figure 7. Logarithm of error between the exact and the numerically computed magnetic field perturbation as a function of the logarithm of the number of triangles for points inside the sphere located at different distances from the center of the sphere of radius R.

This is in complete agreement with the results of the error analysis given in Section 3.2. One can see from Figure 6 that the constant of proportionality between the error and $1/N$ varies as a function of the distance to the sphere. This is in connection with the fact that the intensity of the magnetic field perturbation $\mathbf{B}'$ rapidly decreases as the distance to the sphere increases. On the contrary, the constants of proportionality are the same for the three points chosen inside the ball since the magnetic field perturbation $\mathbf{B}'$ is constant inside the ball. As mentioned in the error analysis, the integrand Φ_P behaves like $1/d^2$ where d is the distance from P to the interface $\partial\Omega_k$. The consequence is a lesser accuracy of the method for points at a distance of the boundary comparable to h. This explains in Figure 7 the behavior of the curve for the point the closest to the boundary for small values of N. Such points inside the ball and closed to the boundary do not "view" the boundary approximation with the same accuracy than the outside points or or than the inside points far from the boundary. As a consequence, they are more sensible to the surface approximation. However, even if the error is more important for small values of N, it lessens quickly as N increases. Finally, these results illustrate the fact that the error in our method depends only on the surface approximation and decreases linearly with the number of triangles. The numerical precision of the method can be determined in advance when choosing the number of triangles describing the boundaries.

4.3. Computation Time and Parallelization

Equation (18) clearly shows that the computation of the magnetic field perturbation $\mathbf{B}'$ in a point P is obtained by a summation over the triangles of the triangulation. As a consequence, the computation time τ_p needed to evaluate $\mathbf{B}'$ in one point depends linearly of the time τ_K required to compute the integral over one triangle in the following way:

$$\tau_p = N \times \tau_K, \tag{53}$$

where N is the number of triangles in the triangulation of the boundaries. The total time T needed to compute the magnetic field perturbation $\mathbf{B}'$ in a volume of interest involving $(X \times Y \times Z)$ voxels is given by

$$T = X \times Y \times Z \times N \times \tau_K. \tag{54}$$

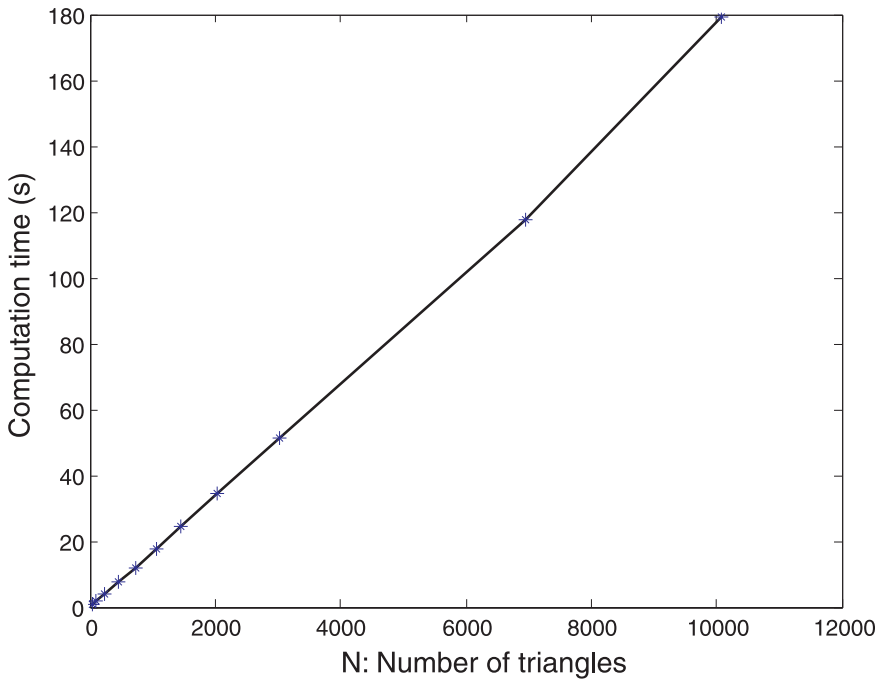

Figure 8. Computation time of the magnetic field perturbation in 256 points on Pentium IV 2.4 Ghz computer as a function of the number of triangles.

This linear dependence of the computation time on the number of triangles is illustrated in Figure 8, where we give the time required to compute the magnetic field perturbation in 256 points for different meshes with an increasing number of triangles.

Since the magnetic field perturbation is computed by summing the contribution of all the triangles of the triangulation, the computation algorithm is simple to parallelize with a "divide and conquer" parallelization scheme. We have implemented a parallel version of the computation method on an 8 PC cluster using MPI (`www-unix.mcs.anl.gov/mpi`). Each node in the cluster receives one eighth of the triangles and computes their contributions (i.e., the related integrals) at each point of the volume of interest. At the end of the process, one node gets all the contributions and sums them. Using this simple parallelization process divides the computation time by a factor equal to the number of computation nodes.

4.4. Test Example of a Hollow Ball

In [20], the authors show that a judicious association of selected paramagnetic and diamagnetic material in a hollow ball can completely cancel the induced magnetic field outside the ball. They propose this dual component approach as a way of reducing artifacts generated by implanted metallic objects. We have tested our method in the case of a hollow ball with the values given in [20]. A spherical shell of titanium (with external radius of 3.6 cm and magnetic susceptibility $\chi_m = 23\ 10^{-4}$) encapsulates a smaller ball of bismuth (with radius of 3.1 cm and susceptibility $\chi_m = -11.9\ 10^{-4}$). This object is magnetized by a static magnetic field $\mathbf{B_0}$ of 1 Tesla. Figure 9 shows the component of the magnetic field perturbation along $\mathbf{B_0}$ on a central slice parallel to $\mathbf{B_0}$ obtained by our computational method when each of the spherical surfaces is meshed with 966 triangles. One can note that outside the ball, the field cancels despite the high magnetic field observed inside the ball. These results are in concordance with those given in [20] and contribute to validate our computation algorithm with two different surfaces corresponding to an interface air/titanium and an interface titanium/bismuth and involving paramagnetic and diamagnetic materials.

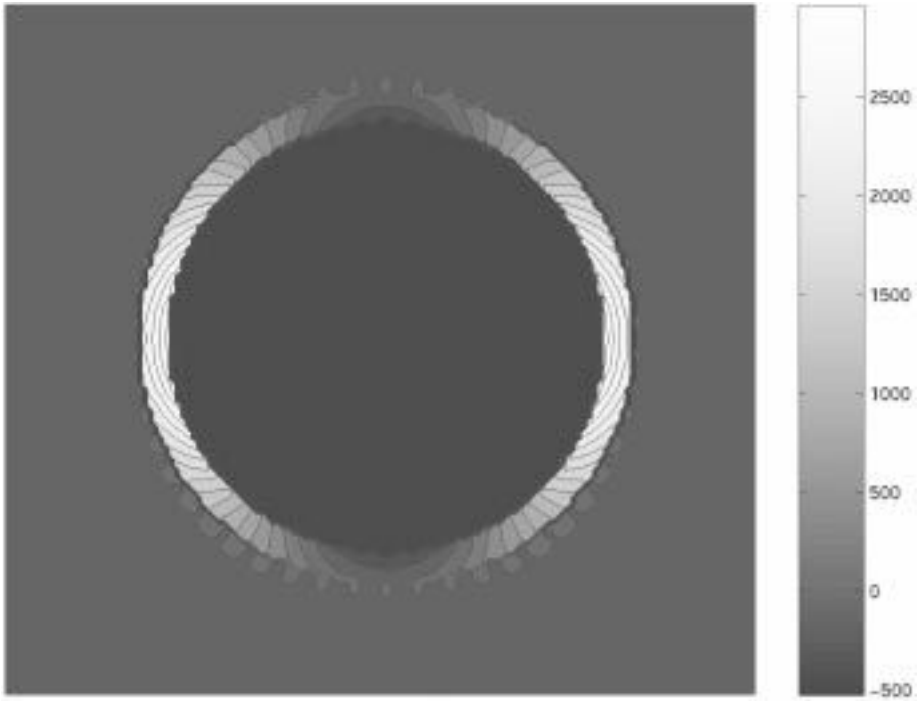

Figure 9. Induced magnetic field (in μT) on a central slice parallel to $\mathbf{B_0}$ for a hollow ball associating titanium ($\chi_m = 23\ 10^{-4}$) and bismuth ($\chi_m = -11.9\ 10^{-4}$.)

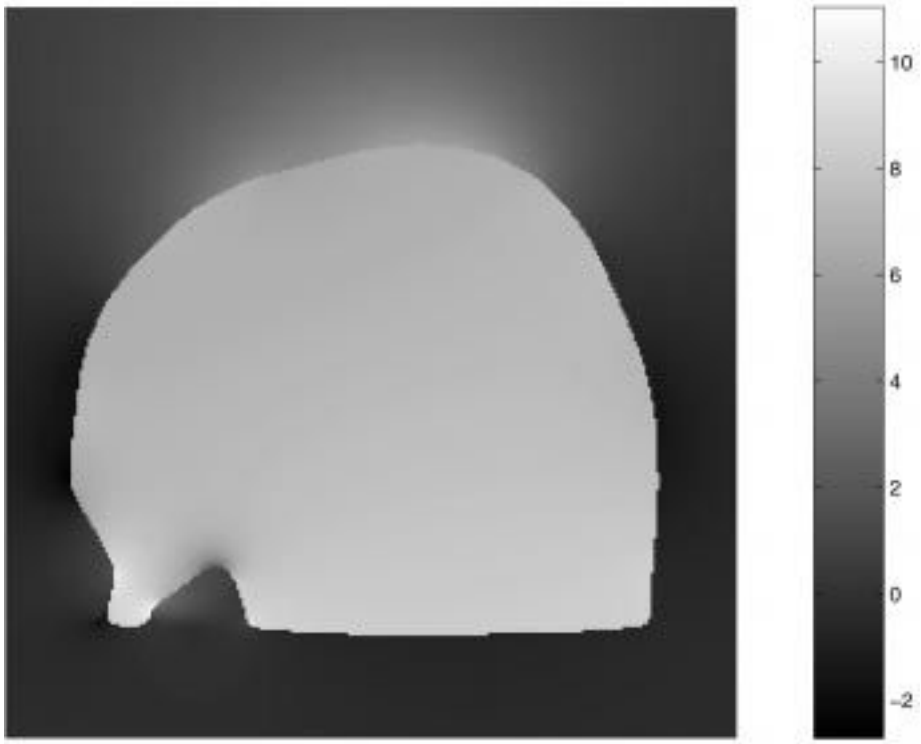

Figure 10. Induced magnetic field in μT on a sagittal slice of the brain crossing the nasal fossa.

4.5. Test on a Human Head

In a last numerical experiment, we have applied our method to compute the field induced by the susceptibility variations between the air and a human head. We use the Montreal brain

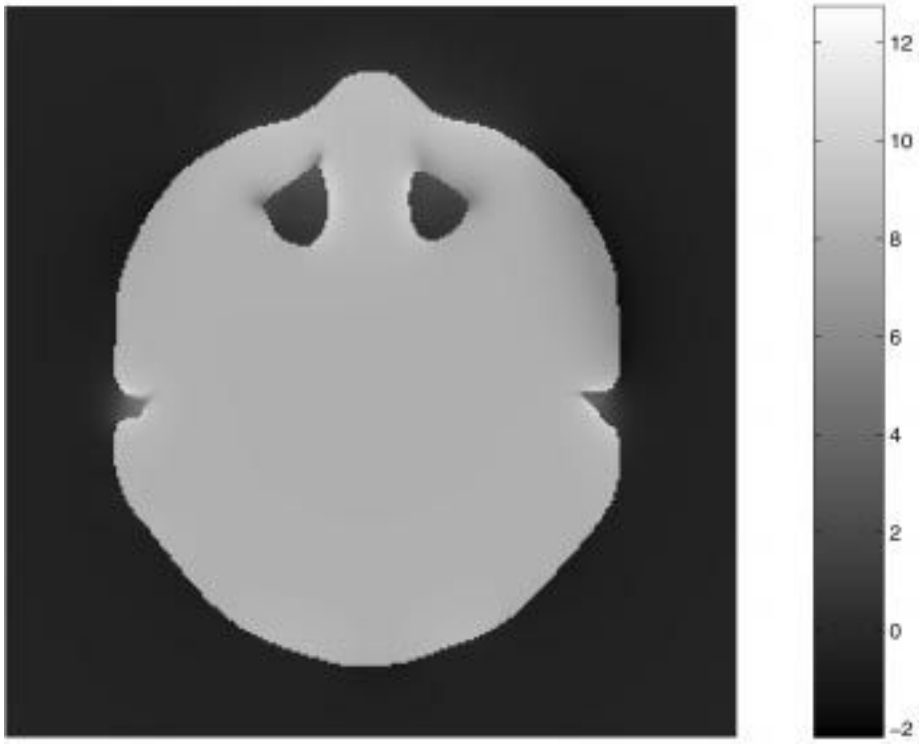

Figure 11. Induced magnetic field in μT on an axial slice of the brain crossing the nasal fossa.

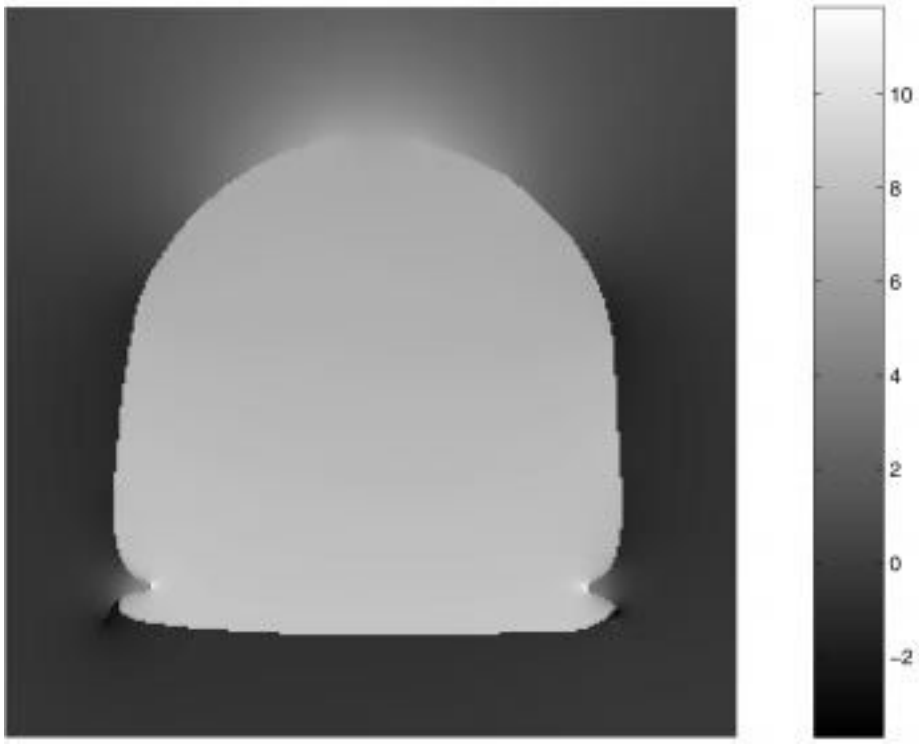

Figure 12. Induced magnetic field in μT on a frontal slice of the brain crossing the internal ears.

phantom [21] and the Marching cube algorithm [22] to get a mesh description by 31064 triangles of the interface head/air including nasal fossa and ears, see Figure 2. Using a single Pentium IV

2.4 Ghz, the computation of the magnetic field perturbation on a slice of 256×256 points requires 20 hours. We present the magnetic field perturbation obtained on a sagittal slice (Figure 10), on a frontal slice (Figure 11), and on an axial slice (Figure 12). These figures clearly show the variation of the magnetic field inside the head due to the high magnetic susceptibility variation between the air in the nasal fossa and the surrounding tissue.

5. CONCLUSION

In this paper, we have proposed an analytic method to compute MRI susceptibility induced magnetic field inhomogeneities. Our approach is based on a description of the susceptibility interfaces. It does not make any assumption on the range of the susceptibility values or on the direction of the static field. The easy parallelization of the method makes the proposed approach usable on a large data set. Furthermore, since the surface integral involved in the perturbed field computation is computed exactly, the perturbed field could be estimated with a given precision by adjusting only the mesh of the involved surfaces. Such a property has to be explored in further works to define a multiresolution method based on multiresolution meshes, see [23,24]. For instance, to compute the perturbed field for points far from the interfaces, a coarse mesh could be used and inversely a fine version of the mesh for points close to the interface.

REFERENCES

1. K.M. Ludeke, P. Roshmann and R. Tischler, Susceptibility artifacts in NMR imaging, *Magnetic Resonance Imaging* **3**, 329–343, (1985).
2. C.J. Bakker, M.A. Moerland, R. Bhagwandien and R. Beersma, Analysis of machine-dependent and object-induced geometric distorsion in 2DFT MR imaging, *Magnetic Resonance Imaging* **10** (4), 597–608, (1992).
3. H. Chang and J.M. Fitzpatrick, A technique for accurate magnetic resonance imaging in the presence of field inhomogeneities, *IEEE Transactions on Medical Imaging* **11** (3), 319–329, (1992).
4. J. Weis, A. Ericsson and S. Silander, Magnetic resonance spectroscopic imaging for visualization and correction of distorsions in MRI: High precision applications in neurosurgery, *Magnetic Resonance Imaging* **16** (10), 1265–1272, (1998).
5. F.M. Bui, K. Bott and M.P. Mintchev, A quantitative study of the pixel-shifting, blurring and nonlinear distortions in MRI images caused by the presence of metal implants, *Journal of Medical Engineering Technology* **24** (1), 20–27, (2000).
6. T. Sumanaweera, G. Glover, S. Song, J. Adler and S. Napel, Quantifying MRI geometric distortion in tissue, *Magnetic Resonance in Medicine* **31**, 40–47, (1994).
7. M. Sadiku, *Numerical Techniques in Electromagnetism*, CRC Press, (1992).
8. R. Bhagwandien, M.A. Moerland, C.J.G. Bakker, R. Beersma and J.J.W. Lagendijk, Numerical analysis of the magnetic field for arbitrary magnetic distribution in 3D, *Magnetic Resonance Imaging* **12**, 101–107, (1994).
9. S. Li *et al.*, A computer simulation of the static magnetic field distribution in the human head, *Magnetic Resonance in Medicine* **34**, 268–275, (1995).
10. T.K. Truong, B.D. Clymer, D.W. Chakeres and P. Schmalbrock, Three dimensional numerical simulations of susceptibility induced magnetic field inhomogeneities in the human head, *Magnetic Resonance Imaging* **20**, 759–770, (2002).
11. M. Jenkinson, J.L. Wilson and P. Jezzard, Perturbation calculation of B0 field for non conducting material, In *10^{th} Annual Meeting of the ISMRM, Volume 2325,* Honolulu, HI, (2002).
12. S.N. Hwang and F.W. Wehrli, The calculation of the susceptibility induced magnetic field from 3D NMR images with applications to trabecular bone, *Journal of Magnetic Resonance* **109**, 126–145, (1995).
13. J.C. de Munck, R. Bhagwandien, S.H. Muller, F.C. Verster and M.B. Van Herk, The computation of MR image distortions caused by tissue susceptibility using the boundary element method, *IEEE Trans. on Medical Imaging* **15** (5), 620–627, (1996).
14. D.A. Yoder, E. Changchien, C.B. Paschal and J.M. Fitzpatrick, MRI simulator with static field inhomogeneity, In *SPIE Medical Imaging, Volume 4684*, pp. 592–603, (2002).
15. S. Balac and G. Caloz, Induced magnetic field computations using a boundary integral formulation, *Applied Numerical Mathematics* **41**, 345–367, (2002).
16. J.D. Jackson, *Classical Electrodynamics*, Third Edition, Wiley, New York, (1999).
17. S. Balac and G. Caloz, Magnetic susceptibility artifacts in magnetic resonance imaging, Calculation of the magnetic field disturbances, *IEEE Transactions on Magnetics* **32**, 1645–1648, (1996).
18. E.E. Okon and R.F. Harrington, The potential integral for a linear distribution over a triangular domain, *International Journal for Numerical Methods in Engineering* **18**, 1821–1828, (1982).

19. S. Chien, Numerical evaluation of surface integrals in three dimensions, *Mathematics of Computation* **64**, 727–743, (1995).
20. B. Chauvel, G. Cathelineau, S. Balac, J. Lecerf and J.D. de Certaines, Cancellation of metal-induced MRI artifacts with dual component paramagnetic and diamagnetic material: Mathematical modelization and experimental verification, *Journal of Magnetic Resonance Imaging* **6**, 936–938, (1996).
21. D.L. Collins, A.P. Zijdenbos, V. Kollokian, J.G. Sled, N.J. Kabani, C.J. Holmes and A.C. Evans, Design and construction of a realistic digital brain phantom, *IEEE Trans. on Medical Imaging* **17** (3), 463–468, (1998).
22. W.E. Lorensen and H.E. Cline, Marching cubes: A high resolution 3D surface construction algorithm, *Computer Graphics* **21** (4), 163–169, (1987).
23. S. Valette, Y.S. Kim, H.Y. Jung, I. Magnin and R. Prost, A multiresolution wavelet scheme for irregularly subdivided 3D triangle mesh, In *IEEE ICIP, Volume I*, KOBE, pp. 171–174, (1999).
24. M. Lounsbery, Multiresolution analysis for surfaces of arbitrary topological type, University of Washington, Ph.D. Dissertation, (1994).